Heliyon 11 (2025) e41202

Contents lists available at ScienceDirect

Heliyon

journal homepage: www.cell.com/heliyon

Research article

PVP-assisted MOF-derived Fe_3O_4/C powders for microwave absorption applications

V. Kavoosi, S.M. Masoudpanah *

School of Metallurgy & Materials Engineering, Iran University of Science and Technology (IUST), Tehran, Iran

ARTICLE INFO

Keywords:
Fe_3O_4
MOF
PVP
Reflection loss
Effective absorption bandwidth

ABSTRACT

Metal-organic framework (MOF) derived porous Fe_3O_4/C powders were applied for absorption of microwaves in the frequency range of 1–18 GHz. The effects of the polyvinylpyrrolidone (PVP) additive on the synthesis of MIL101-(Fe) precursor were studied by various characterization methods. By adding PVP, the impure hematite phase (α-Fe_2O_3) with magnetite phase (Fe_3O_4) was disappeared and the particular morphology was transformed to the porous rod-like, leading to the increase of specific surface area from 150 to 282 m^2/g. Furthermore, the saturation magnetization (Ms) of Fe_3O_4/C powders reached a maximum value of 47 emu/g at a proper amount of PVP. A thin absorber (2.6 mm) made of 50 wt% Fe_3O_4/C powders and 50 wt % paraffine absorbed the whole of X frequency band (8–12 GHz) with a minimum reflection loss of −20 dB at a matching frequency of 10 GHz. Adjusting the permittivity and permeability parameters of the Fe_3O_4/C powders via adding PVP was responsible for their better microwave absorption performance.

1. Introduction

Fifth-generation (5G) networks and wireless telecommunication technologies are rapidly developing for their higher transmission speed and network capacity [1–3]. However, their electromagnetic waves (EMWs) are detrimental to human health and can interfere the performance of electronic devices, demanding the microwave absorber materials (MAMs) for shielding against EMWs. The energy of EMWs can be converted into heat using the magnetic and dielectric MAMs [4,5]. Several MAMs such as graphene, TiO_2, SiO_2, SiC, ZnO, $CoFe_2O_4$, Fe_3O_4, and $BaFe_{12}O_{19}$, are developed for electromagnetic interference shielding applications [6–8]. The absorption performance of various MAMs is usually characterized based on absorption capacity, effective absorption bandwidth (EAB), and matching thickness. A broad EAB at a small matching thickness is suitable for practical applications [9–11].

Magnetic spinel ferrite (MFe_2O_4, M = Fe, Co, Ni, Mn, Zn) and hexagonal ferrite ($MFe_{12}O_{19}$, M = Sr, Ba, Pb) are considered as high-performance MAMs due to their dielectric and magnetic nature [12–14]. Among them, magnetite ($FeFe_2O_4$) has several physico-chemical properties such as high saturation magnetization, high permeability, facile synthesis, and low cost, making it as a notable MAM [15,16]. The spinel structure of Fe_3O_4 is based on a face-centered cubic arrangement of 32 oxygen ions in which the Fe^{3+} and M^{2+} cations are distributed between 16 octahedral [B] and 8 tetrahedral (A) sites [17]. The magnetic and dielectric properties of the Fe_3O_4 powders are mainly tunable by adjusting their phase purity, microstructure, and the cations distribution between (A) and [B] sites through synthesis method [18,19].

Generally, the Fe_3O_4 nanoparticles are synthesized by precipitation method in which the ferric and ferro chlorides are

* Corresponding author.
E-mail address: masoodpanah@iust.ac.ir (S.M. Masoudpanah).

https://doi.org/10.1016/j.heliyon.2024.e41202
Received 11 September 2024; Received in revised form 6 December 2024; Accepted 12 December 2024
Available online 12 December 2024

simultaneously precipitated by adding NaOH agent. However, the low temperature of the precipitation method results in the lower magnetic properties. Therefore, the high-temperature synthesis methods such as solvothermal, thermal decomposition, and solution combustion have been applied for preparing the Fe_3O_4 nanoparticles with high magnetic properties [20–25]. The metal-organic framework (MOF) approach has versatility and tunability in the morphology, pore size, and pore volume of the Fe_3O_4 powders [24]. In the MOF approach, the metal precursors are coordinated by organic ligands such as terephthalic acid, trimesic acid, 1,4-benzene dicarboxylate, etc. in organic solvents to form 1D, 2D, and 3D open structures. The MOF precursor can be then pyrolyzed to the porous materials by exhausting the gaseous products [26–28]. The various MOF-derived materials with high specific surface areas are applied in energy storage and conversion systems, gas sensing, and absorption of EM waves [29–31]. The textural properties of MOF-derived materials are dependent on the synthesis conditions such as the amount and type of ligand and solvent, organic additives, etc. [32,33].

In this work, the effects of the polyvinylpyrrolidone (PVP) additive were studied on the synthesis of MIL101-(Fe) as a precursor for preparing the Fe_3O_4 nanoparticles for microwave absorption applications. The morphology was transformed from particular to rod-like with sheetlike building blocks by adding PVP. The saturation magnetization (Ms) reached a maximum value of 47 emu/g using a proper amount of PVP. The higher Ms value, the higher permeability. The higher microwave absorption performance was attributed to the better impedance matching caused by a proper combination of permittivity and permeability parameters.

2. Experimental procedures

2.1. Materials

Terephthalic acid (H_2BDC) ($C_6H_4(COOH)_2$), ferric chloride hexahydrate ($FeCl_3{\cdot}6H_2O$), PVP ($(C_6H_9NO)_n$, K-30), and N, N-dimethylformamide (DMF) were provided from Merck Chemical Co.

2.2. Synthesis of Fe_3O_4 nanoparticles

The MIL101- (Fe) was prepared by a solvothermal process [34]. Firstly, 1.705 g H_2BDC and 3.581 g $FeCl_3{\cdot}6H_2O$ were completely dissolved in 90.0 mL DMF by magnetic stirring. The various amounts of PVP (1.47 and 2.94 g) were also added to the precursor solution which was then treated in a 100 mL-Teflon-lined stainless reactor at 110 °C for 20 h. The obtained brown precipitates were collected and dried at 60 °C for 3 h. The MIL-101(Fe) powders were transformed into the Fe_3O_4 nanoparticles by pyrolyzing at 650 °C for 2 h under Ar atmosphere with a heating rate of 5 °C min^{-1}. The Fe_3O_4 nanoparticles were coded as P0, P1, and P2 based on the PVP contents.

2.3. Materials characterization

The MOF-derived Fe_3O_4 powders were structurally analyzed on a D8 ADVANCE X-ray diffractometer (Bruker, Japan). The CuKα (λ = 1.540 Å) irradiation was generated at 30 kV and 10 mA for obtaining the diffraction pattern. The diffraction range (2θ = 10°–80°) was scanned in a rate of 0.04°/0.5 s. An X-ray photoelectron spectroscopy (XPS) (BESTEC, EA 10, Germany) was applied for

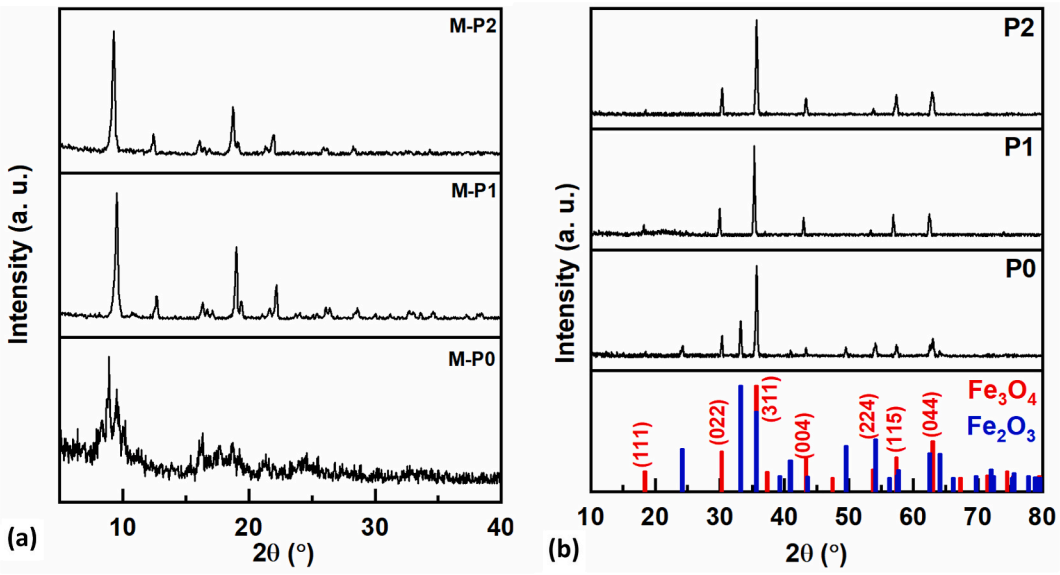

Fig. 1. XRD patterns of (a) MIL-101(Fe) and (b) MOF-derived Fe_3O_4 powders versus PVP contents.

characterizing the valence state of the Fe, O, and C elements in the surface of Fe_3O_4 nanoparticles. The microstructure was observed using VEGA II scanning electron microscopy (TESCAN, Czech Republic). A Tristar 3000 instrument (Micromeritics, USA) was applied for measuring the nitrogen ad/desorption isotherms on the degassed powders at 250C for 5 h. The magnetic properties of the Fe_3O_4 powders were determined on a vibrating sample magnetometer (Meghnatis Daghigh Kavir Co., Iran) at room temperature.

The values of relative permittivity ($\varepsilon_r = \varepsilon'$-j$\varepsilon''$) and permeability ($\mu_r = \mu'$-j$\mu''$) of the toroidal-shaped coaxial sample ($\psi_{out} = 7.0$ mm and $\psi_{in} = 3.04$ mm) were measured on a vector network analyzer (VNA) (Agilent/HP 8722 ES). According to ASTM D7449 standard, the Fe_3O_4 powders were mixed with paraffine (50 wt%) in toluene solvent under sonication. Then the paste was molded and dried at 80 °C in an oven.

3. Results and discussion

XRD patterns of the MIL-101(Fe) and MOF-derived Fe_3O_4 powders versus PVP contents are shown in Fig. 1a. The reflections of MIL-101 are in accordance with the reported patterns for MIL structure which is composed of metal nodes (Fe^{3+}) in carboxylate trimeric clusters [35]. The structure of MIL-101 are independent of PVP additives (Fig. 1a), confirming its high purity. After pyrolyzing, the P0 powders have the reflections of (111), (022), (311), (004), (224), (115), and (044) which are related to the spinel structure of magnetite phase with space group of Fd3m (PDF2#01-075-0449). Furthermore, there are the reflections of α-Fe_2O_3 phase (PDF2#00-039-1346) in the P0 sample which are disappeared by adding the PVP. The ferric (Fe^{3+}) cations are coordinated through oxygen atoms of carboxylic groups which can be decomposed into the hematite (α-Fe_2O_3) phase during calcination at high temperatures. Burning the organic framework releases the CO and H_2 gases which reduce α-Fe_2O_3 to Fe_3O_4. Burning the PVP molecules liberated a large amount of gaseous products such as CO and H_2, benefitting for the complete reduction of α-Fe_2O_3 to Fe_3O_4. The crystallite size and lattice strain were determined from the peak broadening in which the crystallite size decreases from 45 to 33 nm, while the lattice strain increases from −0.1 to +0.2 % by the increase of PVP, indicating their lower crystallinity.

The full XPS spectrum of the P1 sample (Fig. 2a) shows three typical peaks of C1s (284 eV), O1s (531 eV), and Fe2p (711 eV), suggesting the presence of C, O, and Fe elements. The high-resolution XPS spectra show further elemental detailed information. There are two peaks of 711.1 eV and 724.6 eV in the high-resolution Fe2p spectrum (Fig. 2b), respectively corresponding to $Fe2p_{3/2}$ and $Fe2p_{1/2}$ on account of the spin-orbit coupling [36]. The Fe^{3+} species has $Fe2p_{3/2}$ (712.1 eV) and $Fe2p_{1/2}$ (725.4 eV) components with a satellite peak at 716.7 eV [37]. However, a pair of $Fe2p_{3/2}$ (711.5 eV) and $Fe2p_{1/2}$ (723.8 eV) components with a satellite peak at 732.7 eV are related to the Fe^{2+} species [38]. As shown in the O1s spectrum in Fig. 2c, the two peaks at 530.28 and 528.92 eV are respectively corresponded to Fe−O−C and Fe−O species [39], meaning that there is some residual carbon on the Fe_3O_4 nanoparticles.

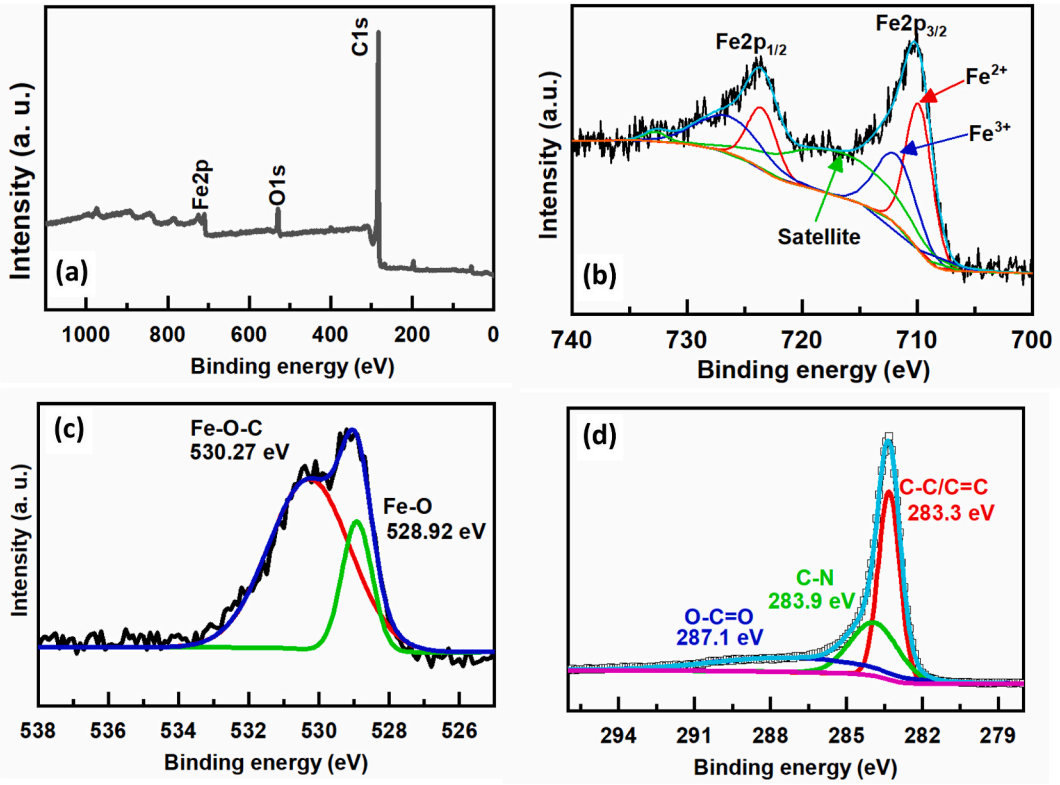

Fig. 2. (a) full XPS spectra of the P1 sample and high-resolution XPS spectra; (b) Fe2p, (c) O1s, and (d) C1s.

Fig. 2d is the C1s spectrum. The binding energy values of 283.30, 283.9, and 287.1 eV are due to the C=C/C−C, C-N, and O-C=O species, respectively [17,40] caused by depositing carbon on the Fe_3O_4 nanoparticles through burning the organic framework and PVP molecule.

SEM images of the MOF-derived Fe_3O_4 powders are shown in Fig. 3. The P0 powders are composed of the Fe_3O_4 nanoparticles (~40 nm) agglomerated on the pores' walls. Burning the organic framework is responsible for the macropores. By adding the PVP, the morphology is transformed from a particular to a rod-like with sheetlike building blocks (Fig. 3c1 and c2). The octahedral morphology of MIL101-(Fe) can be modified by adding PVP. The entanglement of PVP molecules geometrically confine the growth of MIL101-Fe, leading to the elongated octahedral particles as rod-like particles. Furthermore, the PVP additive changes the decomposition rate of MIL101-(Fe) molecules, inducing the sheet-like building blocks [41].

N_2 ad/desorption isotherms of the MOF-derived Fe_3O_4 powders are presented in Fig. 4a. The fragile agglomeration of Fe_3O_4 nanoparticles result in the IV type isotherm with H3 hysteresis. The values of BET specific surface area are 150, 206, and 282 m^2/g for the P0, P1, and P2 samples, respectively. Furthermore, the pore volume slightly increases from 0.50 cm^3/g for the P0 sample to 0.55 and 0.53 cm^3/g for the P1 and P2 samples, respectively. The higher specific surface area of the PVP-assisted samples can be attributed to the morphological evolution from particular to rod-like with sheetlike building blocks. The rod-like morphology has the lower packing density, inducing the higher specific surface area. The average size of pores is centered about 10 nm, showing their mesopores' nature. The pyrolysis of the organic materials leads to the gaseous products, inducing the micropores and macropores.

Magnetization curves of the MOF-derived Fe_3O_4 powders are shown in Fig. 5. The porous powders show S-shaped curve with a hysteresis loop, corresponding to their ferromagnetic behavior. The Fe_3O_4 phase has a spinel structure in which the magnetic Fe^{3+} and Fe^{2+} cations are distributed between tetrahedral (A) and octahedral [B] sites [42]. The reversely exchange-coupling of Fe^{3+} and Fe^{2+} cations via oxygen ions is responsible for the magnetic moments and saturation magnetization of Fe_3O_4 phase. The unequal magnetic moments of Fe^{3+} and Fe^{2+} results in the spontaneous magnetization of the Fe_3O_4 phase as similar to the ferromagnetic materials with magnetic hysteresis loop [43]. The values of saturation magnetization (Ms) and coercivity (Hc) are dependent on the PVP contents. With the increase of PVP, the Ms value first increases from 16 to 47 emu/g and then decreases up to 41 emu/g. The coercivity decreases from 163 to 155 Oe by adding PVP. The magnetic properties are related to the phase purity, cation distribution, particle size and shape [44–46]. With the increase of PVP, the Ms value first increases from 16 to 47 emu/g and then decreases up to 41 emu/g. The disappearance of nonmagnetic α-Fe_2O_3 phase is responsible for the increase of Ms value. However, the decrease of Ms can be attributed to the spin canting effects [47–49]. The disorderings of magnetic moments at the surface of Fe3O4 nanoparticles lead to the decrease of saturation magnetization.

The permittivity, permeability, and dielectric and magnetic loss factors of the MOF-derived Fe_3O_4 powders are presented in Fig. 6. The real permittivity (ε′) of the P0 sample decreases from 26 to 7.7 in the frequency range of 1–18 GHz. By adding the PVP, the average value of ε′ decreases from 16 to 4 (Fig. 6a). Consequently, there is similar trend for imaginary permittivity (ε") versus frequency (Fig. 6b) in which the ε" value is sharply decreased in lower frequency region (1–4 GHz) and then it is slowly decreased at higher frequencies. The average ε" value decreases from 11 to 0.5 by adding the PVP. Furthermore, the ε" spectra show a broad peak in at the

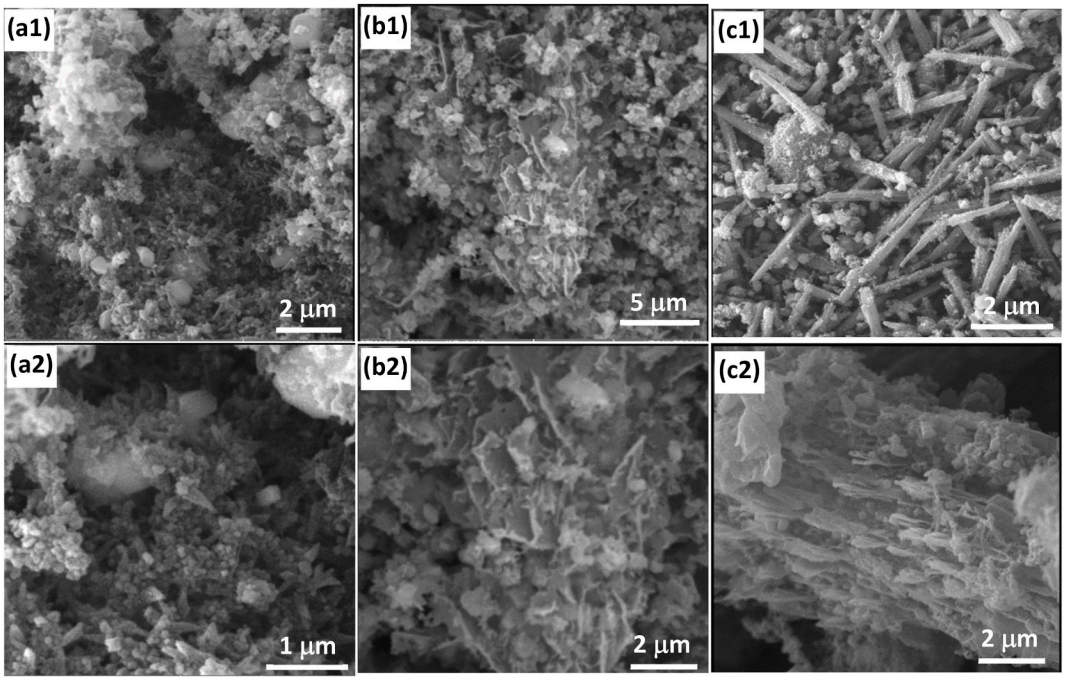

Fig. 3. SEM images of the MOF-derived Fe_3O_4 powders; (a1 and a2) P0, (b1 and b2) P1, and (c1 and c2) P2.

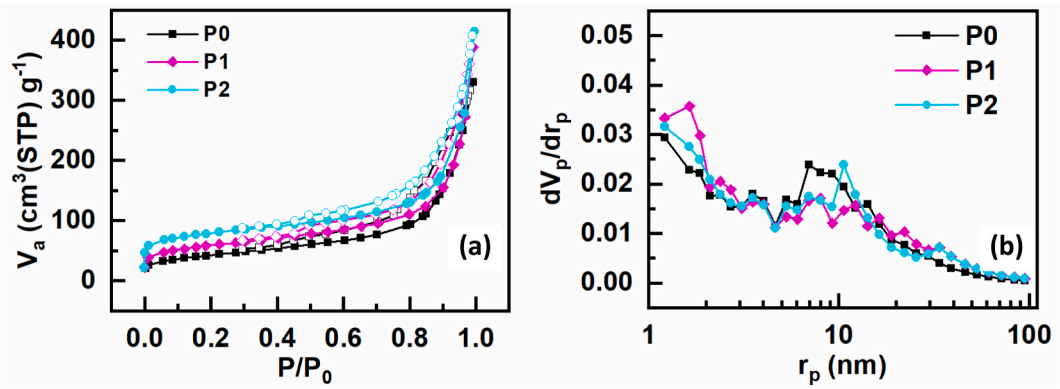

Fig. 4. (a) ad/desorbed volume of N_2 versus relative pressure and (b) pore size distribution plots.

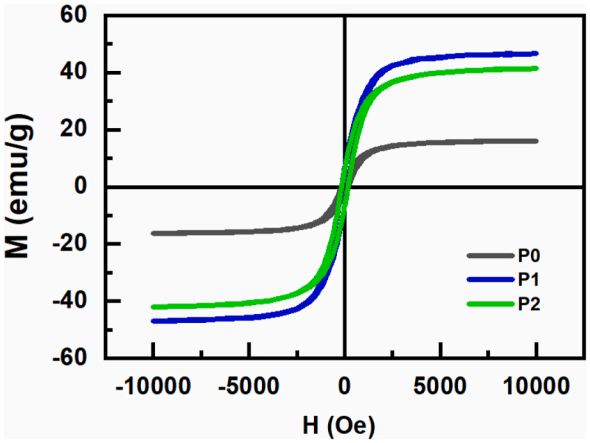

Fig. 5. Hysteresis loops of the MOF-derived Fe_3O_4 powders versus PVP contents.

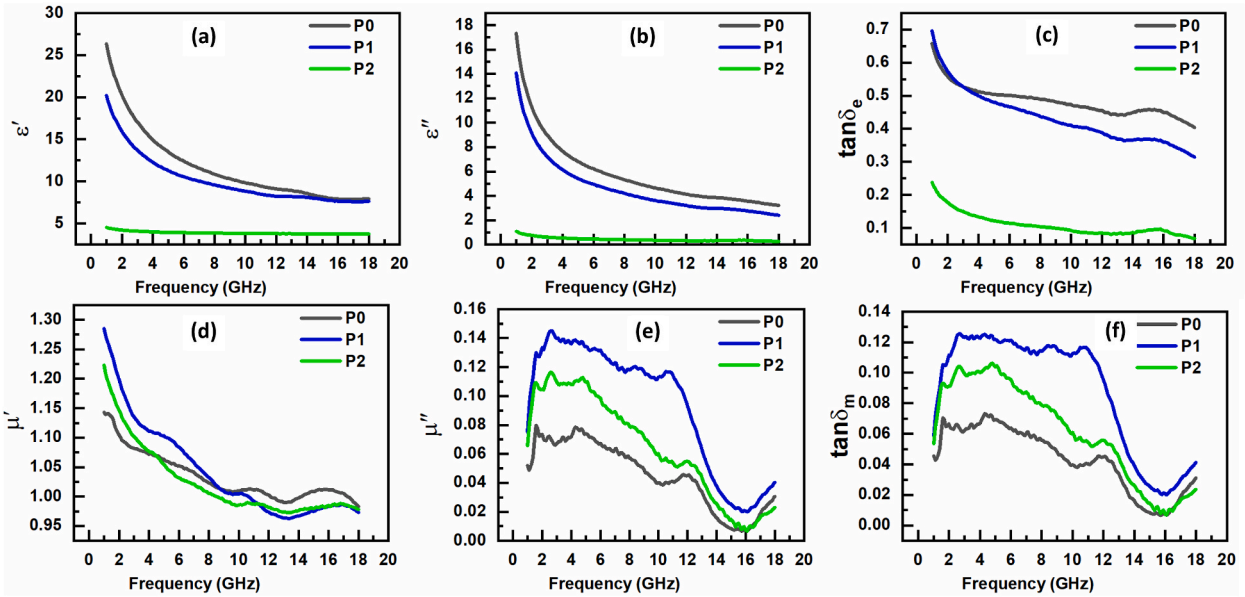

Fig. 6. (a) Real permittivity, (b) imaginary permittivity, (c) dielectric loss factor, (d) real permeability, (e) imaginary permeability, and (f) magnetic loss factor.

frequency range of 12–18 GHz. This broad peak is clearly observable in the dielectric loss factor (Fig. 6c). The permittivity spectra can be described based on conduction loss and dipolar polarization phenomena as dielectric loss mechanisms [50]. The higher contribution of conduction loss mechanism leads to the initial substantial decrease of permittivity in the low-frequency region [51]. The flow of electrons in the absorber by incident EMWs is responsible for the conduction loss mechanism. Therefore, the imaginary part (ε") of permittivity as a loss capacity is directly proportional to the electrical conductivity ($\sigma = \sigma_{ac}+\sigma_{dc}$) as follows [52]:

$$\varepsilon'' = \frac{\sigma}{2\pi f \varepsilon_0} = \frac{\sigma_{ac}}{2\pi f \varepsilon_0} + \frac{\sigma_{dc}}{2\pi f \varepsilon_0} \quad (1)$$

which f is frequency of EMWs and ε_0 is vacuum permittivity. The higher contribution of the DC electrical conductivity (σ_{dc}) than that of the AC conductivity (σ_{ac}) leads to the initial drop in ε" values. The term of $\frac{\sigma_{ac}}{2\pi f \varepsilon_0}$ has a constant value because the σ_{ac} is proportional to the frequency (f). The broad peak on the ε" spectra is due to the dipolar polarization mechanism. Among various origins of dipolar polarization, the space charge distribution mechanism is more common for polycrystalline materials. The mobile charges can be accumulated at phase interfaces and grain boundaries, leading to the interfacial dipoles as space charge distribution. According the Debye model, the electrical energy of EMWs is attenuated by fluctuating the interfacial dipoles [53,54]. The lower permittivity of the P2 powders can be attributed to the porous microstructure of rod-like particles. These pores decrease the electrical conductivity through the reduction of packing density.

Fig. 6d and e shows the dependence of the real (μ') and imaginary (μ") parts of permeability spectra versus frequency. All samples show relatively similar values of μ' at the whole frequency range (1–18 GHz) in which the μ' values decrease from 1.35 to 0.95 due to the deviation of magnetic dipoles' vibrations from alternating applied fields [55,56]. The μ" spectra have several broad peaks in the frequency range of 1–16 GHz caused by the various mechanisms of the ferromagnetic resonance. The natural resonance occurs at below 10 GHz, while the exchange resonance become active at above 10 GHz [50]. Moreover, the average value of μ" first increases from 0.03 to 0.09 and then decreases to 0.06 with adding the PVP. The permeability values are dependent on the saturation magnetization and magnetic anisotropy of the Fe_3O_4/C powders which can be adjusted by the PVP contents. Fig. 6f shows the magnetic ($\tan\delta_m$) loss factors versus frequency which is similar to the μ" spectra. However, the dielectric loss factor ($\tan\delta_e$) (0.1–0.7) is higher than that of magnetic loss factor ($\tan\delta_m$) (0–0.13), showing the higher contribution of dielectric loss in comparison with the magnetic loss.

Fig. 7 shows the dependence of reflection loss (RL) on frequency and absorber thickness. The reflection loss (RL) can be calculated using the normalized input impedance (Z_{in}/Z_0) as follows [57]:

$$RL(dB) = 20\, log\left|\frac{\frac{Z_{in}}{Z_0}-1}{\frac{Z_{in}}{Z_0}+1}\right| \quad (2)$$

$$\frac{Z_{in}}{Z_0} = \sqrt{\frac{\mu_r}{\varepsilon_r}}\tanh\left(j\left(\frac{2\pi f t}{c}\right)\sqrt{\mu_r \varepsilon_r}\right) \quad (3)$$

which Z_0 is free space impedance, f is frequency, t is absorber thickness, also known as matching thickness, ε_r is relative permittivity, and μ_r is relative permeability [58]. An efficient microwave absorber has the deep reflection loss, broad effective absorption bandwidth (EAB) (reflection loss < -10 dB), and small matching thickness. The P0 powders show strong absorption of −34 dB at a matching thickness of 1.6 mm in Ku band. By adding PVP, the minimum RL increases up to −42 dB at a matching frequency of 13 GHz for the matching thickness of 2.1 mm. However, the absorption capacity worsens for the P2 sample with the minimum RL of −13 dB at high-frequency regions (X and Ku bands) and high matching thicknesses (10 mm).

The dependence of EAB on the matching thickness for the P0 and P1 samples is presented in Fig. 8a. The EAB vs. matching thickness has a similar trend in which EAB first sharply increases up to a maximum and then gradually decreases with the increase of matching thicknesses. At the higher matching thicknesses of 2 mm, the P1 sample has a broader EAB than the P0 powders. The P0 absorber has an EAB of 5.9 GHz in the Ku band (12–18 GHz) at a matching thickness of 1.8 mm. However, the P1 sample can effectively absorb 85 % (5.1 GHz) Ku band at a matching thickness of 1.9 mm. The P1 sample shows an EAB of 4.3 (8–12.3) GHz in X band at a matching

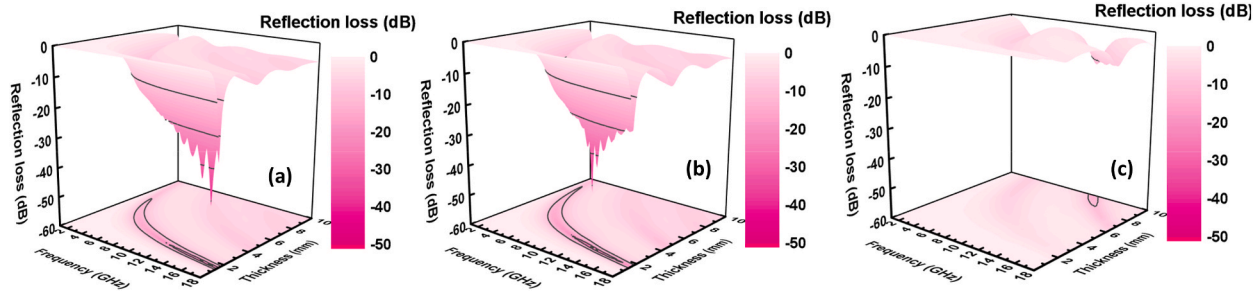

Fig. 7. Dependence of RL values on matching frequency and matching thickness for the MOF-derived Fe_3O_4 powders; (a) P0, (b) P1, and (c) P2.

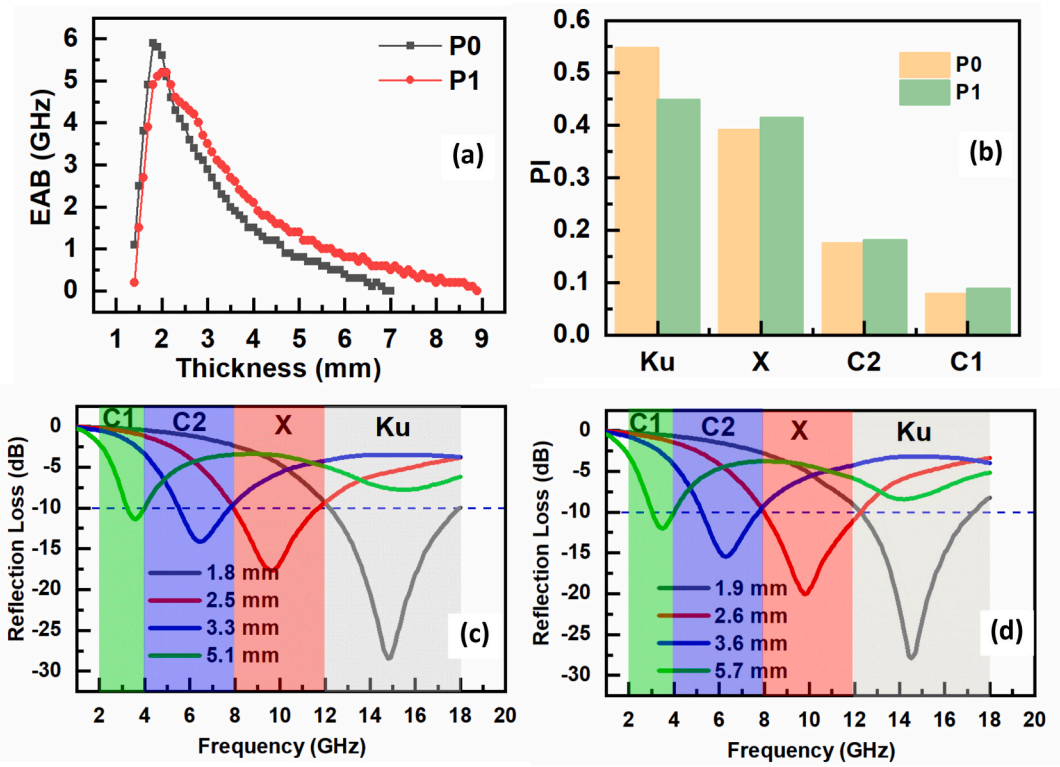

Fig. 8. (a) EAB vs. matching thickness, (b) PI for various frequency band, and reflection loss curves at the matching thicknesses which results in the broad EAB for (c) P0 and (d) P1 samples.

thickness of 2.6 mm. A predominance index (PI) for each frequency band is defined as follows [59]:

$$PI = \frac{EAB}{\Delta f_{band} \times t_m} \tag{4}$$

which t_m is matching thickness and Δf_{band} is the bandwidth of frequency band. The large PI value as a crucial characteristic of the high-performance MAMs is caused by the broad EAB at the small thicknesses. Fig. 8b compares the PI values of the P0 and P1 powders for the different frequency bands. The low-frequency bands have lower PI values. Except of Ku band, the P1 powders have the higher PI values than that of P0 sample. Fig. 8c and d presents the reflection loss curves at the matching thicknesses which show the broad EAB in the frequency band. The P0 and P1 powders effectively absorb the EMWs at small matching thicknesses. However, the minimum reflection loss decreases at the low-frequency bands in which the suitable matching thicknesses are high. The microwave absorption performance of the various Fe_3O_4-based materials is compared in Table 1 by regarding the EAB, matching thickness, and minimum reflection loss. The MOF derived Fe_3O_4 powders offer the higher microwave performance due to the adjustment of permittivity and permeability values by adding PVP. Furthermore, the higher microwave performance of MOF-derived Fe_3O_4 powders can be attributed to the structural and microstructural features including the high crystallinity, small nanoparticles, and porosity.

The dielectric and magnetic loss mechanisms are responsible for the microwave absorption performance. In the microwave range, the conduction loss and dipolar polarization are active mechanisms of dielectric loss [6]. The dipolar polarization can be modeled by the following Debye equation [61,62]:

Table 1
Microwave absorption performance of the Fe_3O_4-based composites.

Material	EAB_{max} (GHz)	t_m (mm)	RL_{min} (dB)	PI @ band	Fill ratio (mass %)	Refs.
Fe_3O_4/rGO	3.8	1.7	−15	0.55@X	60	[25]
Fe_3O_4/NPC/rGO	5.5	2	−72.6	0.45@Ku	25	[42]
Fe_3O_4/Ppy	5.12	2.5	−40.53	0.34@Ku	–	[17]
Fe_3O_4/C	4.5	3	−65.6	0.37@X	40	[45]
Fe_3O_4/Graphene foam	6.7	2.5	−45.08	0.44@Ku	–	[36]
Fe_3O_4/C/Ppy	4.16	2.13	−53.7	0.29@Ku	–	[60]
Fe_3O_4 (P1)	4.3	2.6	−42	0.41@X	50	This work

$$\varepsilon_r = \varepsilon' - j\varepsilon'' = \varepsilon_{r\infty} + \frac{\varepsilon_{r0} - \varepsilon_{r\infty}}{1 + j\omega\tau} \quad (5)$$

which τ is the relaxation time, $\omega = 2\pi f$ is the operating angular frequency, and ε_{r0} and $\varepsilon_{r\infty}$ are the permittivity values at low and high frequencies, respectively. By removing the frequency ($\omega = 2\pi f$) parameter, the Debye equation is transformed to a circle's equation in ε'' vs. ε' space (Cole-Cole plot) as follows [63,64]:

$$\left(\varepsilon' - \frac{\varepsilon_s - \varepsilon_\infty}{2}\right)^2 + (\varepsilon'')^2 = \left(\frac{\varepsilon_s - \varepsilon_\infty}{2}\right)^2 \quad (6)$$

Fig. 9a shows the Cole-Cole plots. There are semicircles and inclined linear regions which are respectively due to the dipolar polarization and the conduction loss [65]. The dipolar polarization is categorized on the base of dipoles' origin; the orientational, spontaneous, space charge, and interfacial polarization. In the polycrystalline and composite powders, the interfacial relaxation are mainly active due to a plenty of phase interfaces [66]. A wide region of inclined linear in the Cole-Cole plot indicates the higher contribution of conduction loss in the P0 and P1 powders. However, the lower contribution of conduction loss in the P2 powders leads to the shorter linear part. The porous rod-like morphology of P2 sample is responsible for the lower packing density and then the lower conductivity. In other words, the microwave absorption performance is weakened by changing the morphology from particular to rod-like because of the weakening of the conduction loss, leading to the lower permittivity.

The ferromagnetic resonance and eddy-current effect are two main mechanisms for magnetic loss in the microwave range [67]. Several broad peaks in μ" spectra (Fig. 6e) are due to the ferromagnetic resonance phenomena in the Fe_3O_4 nanoparticles. The ferromagnetic resonance frequency of bulk Fe_3O_4 is in the MHz range due to the low anisotropy field of its spinel structure [68]. However, the Fe_3O_4 nanoparticles have the higher anisotropy field due to the surface anisotropy [69]. The Fe_3O_4 nanoparticles have the higher surface disorders due to the higher atoms at their surface. Therefore, the Fe_3O_4 nanoparticles with higher magnetic anisotropy show the resonance frequency in the GHz region [68]. The contribution of eddy current loss can be determined by considering the dependence of $\mu''\mu'^{-2}f^{-1} = 2\pi\mu_0 d^2\sigma = C_0$ values on frequency (f) [7], as shown in Fig. 9b. In the frequency range that the C_0 values remain constant, the magnetic loss mechanism is eddy-current effect. The P0, P1, and P2 samples have similar trends of C_0 values. The C_0 values first decrease and then become constant at above 14 GHz, indicating the predominance of the eddy-current effect in the high-frequency region. The attenuation of EMWs per unit distance inside the absorber is determined by the attenuation (α) coefficient which is related to the permittivity and permeability parameters as follows [70]:

$$\alpha = \frac{\sqrt{2}\pi f}{c}\sqrt{(\mu''\varepsilon'' - \mu'\varepsilon') + \sqrt{(\mu''\varepsilon'' - \mu'\varepsilon')^2 + (\mu'\varepsilon'' + \mu''\varepsilon')^2}} \quad (7)$$

Fig. 9c shows the α coefficient vs. frequency. The P0 powders have the α values in the range of 38–225. However, by decreasing the permittivity values, the maximum of α values decreases to 180 and 33 for the P1 and P2, respectively.

For a high-performance MAM, the values of permittivity and permeability provide the impedance matching between the free space (Z_0) and absorber (Z_{in}), i.e., $Z_0 = Z_{in}$ [71,72]. By matching the impedances, the EMWs are not reflected from the surface of absorber, and then the incident EMWs easily enter into the absorbers. The frequency and thickness for matching the impedances can be evaluated by regarding two criteria; (1) the further closeness of $|Z| = |Z_{in}/Z_0|$ to ~1, the better impedance matching [73] and (2) the smaller delta-function, $|\Delta| = |\sinh^2(Kfd) - M|$, the better the impedance matching. The real values of K and M are determined as follows [74]:

$$K = \frac{4\pi\sqrt{\varepsilon'\mu'}}{c}\frac{\sin\left(\frac{\delta_e + \delta_m}{2}\right)}{\cos\delta_e \cos\delta_m} \quad (8)$$

$$M = \frac{4\mu' \cos\delta_e \times \varepsilon' \cos\delta_m}{(\mu' \cos\delta_e - \varepsilon' \cos\delta_m)^2 + \left(\tan\left(\frac{\delta_m - \delta_e}{2}\right)\right)^2 (\mu' \cos\delta_e + \varepsilon' \cos\delta_m)^2} \quad (9)$$

Fig. 10 shows the 2D contours of |Z| and |Δ| values versus thickness and frequency. The matching impedance region ($0.5<|Z|<1.5$ and $|\Delta|<0.4$) is narrow for the P0 powders (Fig. 10a and b). By adding PVP, the absorber and free-space impedances are matched at the broader ranges of frequency and thickness (orange region) due to the decrease of permittivity (Fig. 10c and d). However, the P2 powders with very low permittivity satisfy the impedance matching condition ($|Z|\sim1$) in a linear region (Fig. 10e). Furthermore, there is no region of frequency and thickness for delta-function condition ($|\Delta|<0.4$) by the P2 powders, indicating the reflection of incident EMWs. Therefore, the very weak microwave absorption performance of the P2 powders is caused by the mismatching of impedance.

In summary, the high magnetic properties of the Fe_3O_4 phase are helpful for the magnetic loss through the ferromagnetic resonance and eddy-current mechanisms [75,76]. The high electrical conductivity of Fe_3O_4 is also benefitted for the conduction loss. However, the change of morphology from particular to rod-like by adding high amounts of PVP decreases the permittivity through weakening the conductivity. Furthermore, the contribution of interfacial relaxation in dielectric loss is lower than the contribution of conduction loss, as shown by Cole-Cole plot. Therefore, the rod-like morphology shows the weak absorption performance due to the very low permittivity, leading to the impedance mismatching. However, the proper amounts of PVP additive increase the permeability, leading to the higher microwave absorption performance through matching the impedances. Furthermore, the deposited carbon on the Fe_3O_4 nanoparticles can increase the electrical conductivity and dielectric loss. However, there is a contrasting trend of downsizing Fe_3O_4

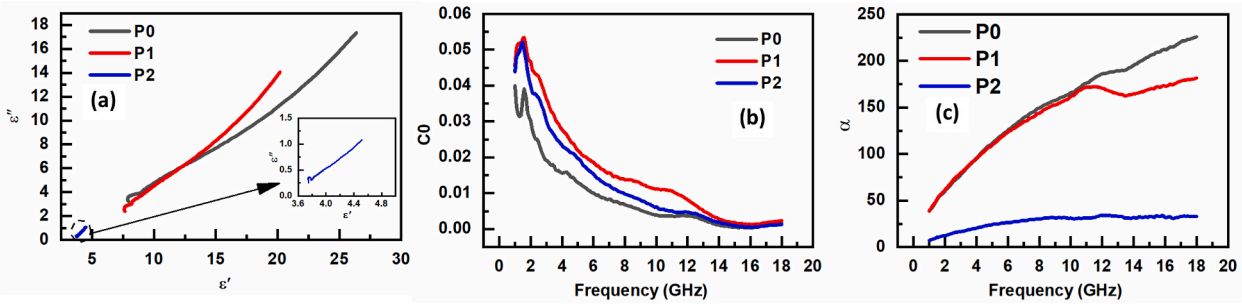

Fig. 9. (a) Cole-Cole plots, (b) C0 versus frequency, and (c) attenuation coefficient vs. frequency.

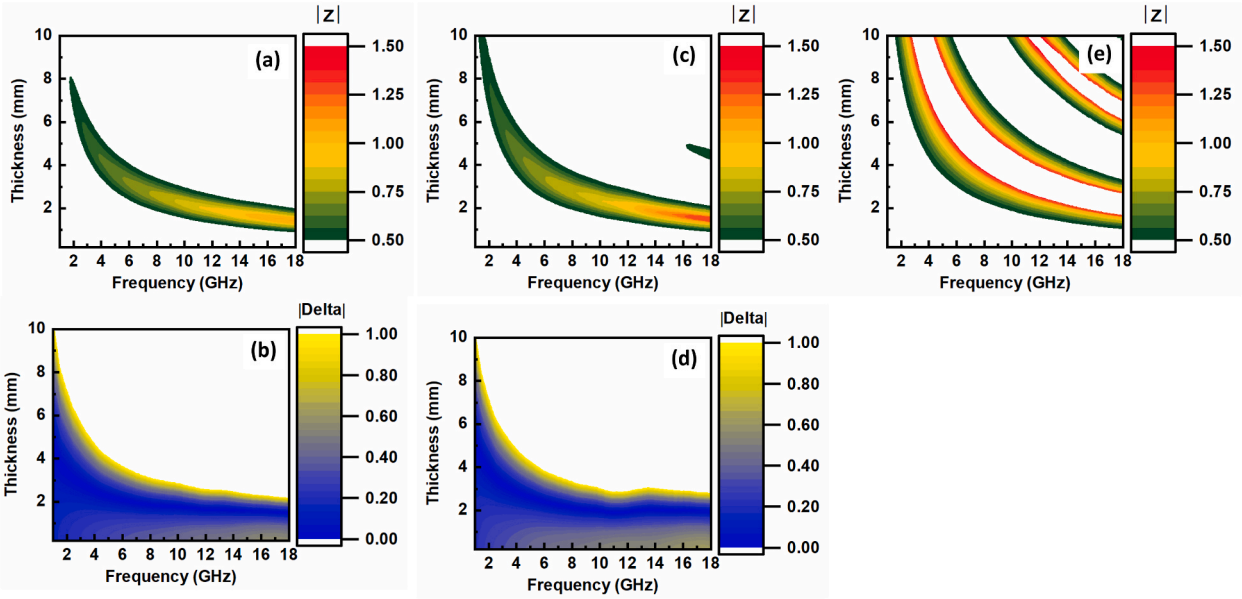

Fig. 10. Contour of |Z| and |Δ| values versus thickness and frequency for (a and b) P0, (c and d) P1, and (e) P2.

nanoparticles. At the higher PVP additives, the higher deposited carbon, but the average size of Fe_3O_4 nanoparticles decreased. The higher deposited carbon led to higher electrical conductivity, while the smaller particle size decreased the conductivity. In other words, despite the higher residual carbon at the P2 sample, its conductivity was lower due to its very small particle size.

4. Conclusion

The MOF approach was modified by adding PVP for preparing the porous $Fe_3O_{4/C}$ powders. The application of PVP led to the morphology transformation from particular to rod-like which increased the specific surface area from 150 to 282 m^2/g. By adding the PVP, the saturation magnetization increased from 16 to 47 emu/g due to the disappearance of antiferromagnetic α-Fe_2O_3 phase and improvement of the crystallinity. Despite the decrease of permittivity values, the permeability first increased and then decreased with PVP content. By approaching the permittivity and permeability, the microwave absorption performance of the $Fe_3O_{4/C}$ powders improved at a proper amount of PVP additive.

CRediT authorship contribution statement

V. Kavoosi: Formal analysis, Data curation, Conceptualization. **S.M. Masoudpanah:** Writing – review & editing, Writing – original draft, Supervision, Conceptualization.

Declaration of competing interest

The authors declare that they have no known competing financial interests or personal relationships that could have appeared to

influence the work reported in this paper.

Appendix A. Supplementary data

Supplementary data to this article can be found online at https://doi.org/10.1016/j.heliyon.2024.e41202.

References

[1] S. Sharma, et al., Progress in microwave absorbing materials: a critical review, Adv. Colloid Interface Sci. 327 (2024) 103143.
[2] B. Li, et al., Metal sulfides based composites as promising efficient microwave absorption materials: a review, J. Mater. Sci. Technol. 104 (2022) 244–268.
[3] W. Zheng, et al., Recent progress in iron-based microwave absorbing composites: a review and prospective, Molecules 27 (13) (2022) 4117.
[4] F. Ruiz-Perez, et al., Carbon-based radar absorbing materials: a critical review, J. Sci.: Advanced Materials and Devices 7 (3) (2022) 100454.
[5] R. Peymanfar, et al., Graphite-like carbon nitride (g-C3N4): a promising microwave absorber, Ceram. Int. 48 (12) (2022) 16461–16476.
[6] H. Lv, et al., Electromagnetic absorption materials: current progress and new frontiers, Prog. Mater. Sci. 127 (2022) 100946.
[7] C. Li, et al., Outstanding electromagnetic wave absorption performance of polyacrylonitrile-based ultrahigh modulus carbon fibers decorated with CoZn-bimetallic ZIFs, J. Alloys Compd. 950 (2023) 169912.
[8] H. Liu, et al., Porous cobalt ferrite microspheres decorated two-dimensional MoS2 as an efficient and wideband microwave absorber, J. Alloys Compd. 892 (2022) 162126.
[9] M.F. Elmahaishi, et al., A review on electromagnetic microwave absorption properties: their materials and performance, J. Mater. Res. Technol. 20 (2022) 2188–2220.
[10] K. Chen, et al., Enhanced microwave absorption in graphene-based composites: a study on the synergistic effect of ferrite integration and electromagnetic coupling, Appl. Surf. Sci. 669 (2024) 160531.
[11] X. Yang, et al., Constructing of three-dimensional molybdenum carbide nanoparticles embedded in honeycomb carbon as efficient microwave absorbers, J. Alloys Compd. 1004 (2024) 175732.
[12] J. Ren, et al., Microwave absorption performance evaluation of carbonized derivatives of Fe3O4@MOF-74 with controllable morphologies, ACS Appl. Electron. Mater. 4 (11) (2022) 5221–5233.
[13] G. Fang, et al., Enhanced microwave absorption performance of Fe3O4/Cu composites with coexistence of nanospheres and nanorods, J. Alloys Compd. 817 (2020) 152764.
[14] H. Zhao, et al., The flaky porous Fe3O4 with tunable dimensions for enhanced microwave absorption performance in X and C bands, Nanotechnology 29 (29) (2018) 295603.
[15] X. Xie, et al., Spinel structured MFe2O4 (M = Fe, Co, Ni, Mn, Zn) and their composites for microwave absorption: a review, Chem. Eng. J. 428 (2022) 131160.
[16] X. Luo, et al., *Preparation and excellent electromagnetic absorption properties of dendritic structured Fe_3O_4@PANI composites*, J. Alloys Compd. 891 (2022) 161922.
[17] J. Li, et al., Three-dimensional graphene supported Fe3O4 coated by polypyrrole toward enhanced stability and microwave absorbing properties, J. Mater. Res. Technol. 9 (1) (2020) 762–772.
[18] J. He, et al., N-doped residual carbon from coal gasification fine slag decorated with Fe3O4 nanoparticles for electromagnetic wave absorption, J. Mater. Sci. Technol. 104 (2022) 98–108.
[19] Y. Wang, et al., Co0.2Fe2.8O4/C composite nanofibers with designable 3D hierarchical architecture for high-performance electromagnetic wave absorption, Ceram. Int. 47 (16) (2021) 23275–23284.
[20] I. Castellanos-Rubio, et al., A milestone in the chemical synthesis of Fe3O4 nanoparticles: unreported bulklike properties lead to a remarkable magnetic hyperthermia, Chem. Mater. 33 (22) (2021) 8693–8704.
[21] L.F. Gomez–Caballero, et al., Facile synthesis of Fe3O4 nanoparticles at room temperature coated with meso-2,3-dimercaptosuccinic acid for improved biocompatibility, J. Nanoparticle Res. 25 (4) (2023) 66.
[22] B.A. Eldeeb, W.M.A. El-Raheem, S. Elbeltagi, Green synthesis of biocompatible Fe3O4 magnetic nanoparticles using Citrus Sinensis peels extract for their biological activities and magnetic-hyperthermia applications, Sci. Rep. 13 (1) (2023) 19000.
[23] D. Maity, et al., Synthesis of magnetite nanoparticles via a solvent-free thermal decomposition route, J. Magn. Magn Mater. 321 (9) (2009) 1256–1259.
[24] X. Zhao, et al., Synthesis of magnetic metal-organic framework (MOF) for efficient removal of organic dyes from water, Sci. Rep. 5 (1) (2015) 11849.
[25] A. Tayebi Pak, et al., *Hierarchical porous Fe_3O_4/RGO nanocomposite powders as high performance microwave absorbers*, J. Mater. Res. Technol. 13 (2021) 548–560.
[26] Z. Zhang, et al., A review on metal–organic framework-derived porous carbon-based novel microwave absorption materials, Nano-Micro Lett. 13 (1) (2021) 56.
[27] M. Nozari-Asbemarz, et al., In situ synthesis of Co3O4/CoFe2O4 derived from a metal–organic framework on nickel foam: high-performance electrocatalyst for water oxidation, ACS Appl. Energy Mater. 4 (3) (2021) 2951–2959.
[28] A.J. Howarth, et al., Best practices for the synthesis, activation, and characterization of metal–organic frameworks, Chem. Mater. 29 (1) (2017) 26–39.
[29] W. Wang, et al., A novel MOF-drived self-decomposition strategy for CoO@N/C-Co/Ni-NiCo2O4 multi-heterostructure composite as high-performance electromagnetic wave absorbing materials, Chem. Eng. J. 426 (2021) 131667.
[30] J. Pan, et al., The NiFe2O4/NiCo2O4/GO composites electrode material derived from dual-MOF for high performance solid-state hybrid supercapacitors, Colloids Surf. A Physicochem. Eng. Asp. 609 (2021) 125650.
[31] C. Guan, et al., Rational design of metal-organic framework derived hollow NiCo2O4 arrays for flexible supercapacitor and electrocatalysis, Adv. Energy Mater. 7 (12) (2017) 1602391.
[32] Z. Fereshteh, M. Salavati-Niasari, Effect of ligand on particle size and morphology of nanostructures synthesized by thermal decomposition of coordination compounds, Adv. Colloid Interface Sci. 243 (2017) 86–104.
[33] J. Yan, et al., High-performance electromagnetic wave absorbers based on two kinds of nickel-based MOF-derived Ni@C microspheres, ACS Appl. Mater. Interfaces 11 (43) (2019) 40781–40792.
[34] S. Peng, et al., Preparation of magnetic flower-like carbon-matrix composites with efficient electromagnetic wave absorption properties by carbonization of MIL-101(Fe), J. Magn. Magn Mater. 487 (2019) 165306.
[35] D. Wang, et al., Fe-based MOFs for photocatalytic CO2 reduction: role of coordination unsaturated sites and dual excitation pathways, ACS Catal. 4 (12) (2014) 4254–4260.
[36] Y. Shi, X. Gao, J. Qiu, *Synthesis and strengthened microwave absorption properties of three-dimensional porous Fe_3O_4/graphene composite foam*, Ceram. Int. 45 (3) (2019) 3126–3132.
[37] K. Liu, et al., Effect of Fe3O4 content and microwave reaction time on the properties of Fe3O4/ZnO magnetic nanoparticles, J. Alloys Compd. 781 (2019) 790–799.
[38] J. Feng, et al., Optimization of porous FeNi3/N-GN composites with superior microwave absorption performance, Chem. Eng. J. 345 (2018) 441–451.
[39] B. Qu, et al., Coupling hollow Fe3O4–Fe nanoparticles with graphene sheets for high-performance electromagnetic wave absorbing material, ACS Appl. Mater. Interfaces 8 (6) (2016) 3730–3735.
[40] Yu, J., et al., Facile fabrication of melamine/MXene/FeNi-PBA composite derived multi-interface magnetic carbon foam for high-efficiency microwave absorption. Advanced Electronic Materials. n/a(n/a): p. 2400265.

[41] G. Qin, et al., Tailor the crystal planes of MIL-101(Fe) derivatives to enhance the activity of SCR reaction at medium and low temperature, J. Colloid Interface Sci. 615 (2022) 432–444.
[42] Z. Xiang, et al., *Rational design of 2D hierarchically laminated Fe_3O_4@nanoporous carbon@rGO nanocomposites with strong magnetic coupling for excellent electromagnetic absorption applications*, J. Mater. Chem. C 8 (6) (2020) 2123–2134.
[43] R. Shu, et al., Facile synthesis of nitrogen-doped reduced graphene oxide/nickel-zinc ferrite composites as high-performance microwave absorbers in the X-band, Chem. Eng. J. 384 (2020) 123266.
[44] L.L. Adebayo, et al., *Recent advances in the development of Fe_3O_4-based microwave absorbing materials*, Ceram. Int. 46 (2) (2020) 1249–1268.
[45] Z. Xiang, et al., Enhanced electromagnetic wave absorption of nanoporous Fe3O4 @ carbon composites derived from metal-organic frameworks, Carbon 142 (2019) 20–31.
[46] K. Zhang, et al., Effect of absorbers' composition on the microwave absorbing performance of hollow Fe3O4 nanoparticles decorated CNTs/graphene/C composites, J. Alloys Compd. 748 (2018) 706–716.
[47] S. Lv, et al., Size regulated N-doped carbon encapsulated NiFe alloys/Ni phosphide composites derived from bimetallic Prussian blue analogues for effective microwave absorption, Carbon 218 (2024) 118668.
[48] F. Chen, et al., Bimetallic CoFe-MOF@Ti3C2Tx MXene derived composites for broadband microwave absorption, Chem. Eng. J. 431 (2022) 134007.
[49] D. Shao, et al., Spin canting, metamagnetism, and single-chain magnetic behaviour in a cyano-bridged homospin iron(ii) compound, Chem. Commun. 51 (21) (2015) 4360–4363.
[50] X. Li, et al., In situ synthesis of hierarchical rose-like porous Fe@C with enhanced electromagnetic wave absorption, J. Mater. Chem. C 6 (3) (2018) 558–567.
[51] R. Peymanfar, et al., Recent advances in microwave-absorbing materials fabricated using organic conductive polymers, Frontiers in Materials 10 (2023).
[52] T. Jia, et al., Interface engineering and impedance matching strategy to develop core@shell urchin-like NiO/Ni@carbon nanotubes nanocomposites for microwave absorption, J. Mater. Sci. Technol. 176 (2024) 1–12.
[53] J. Hu, et al., Facile synthesis of FeNi nanoparticle-loaded carbon nanocomposite fibers for enhanced microwave absorption performance, J. Mater. Sci. Technol. 175 (2024) 141–152.
[54] X. Wen, et al., Green carbonization of waste coffee grounds into porous C/Fe hybrids for broadband and high-efficiency microwave absorption, J. Mater. Sci. Technol. 170 (2024) 1–10.
[55] K.C.B. Naidu, M. Wuppulluri, Ceramic nanoparticle synthesis at lower temperatures for LTCC and MMIC technologies, IEEE Trans. Magn. 54 (9) (2018) 1–8.
[56] K. Chandra Babu Naidu, W. Madhuri, Effect of nonmagnetic Zn2+ cations on initial permeability of microwave-treated NiMg ferrites, Int. J. Appl. Ceram. Technol. 13 (6) (2016) 1090–1095.
[57] Y. Li, et al., *Controllable synthesis and enhanced microwave absorbing properties of Fe_3O_4/$NiFe_2O_4$/Ni heterostructure porous rods*, Appl. Surf. Sci. 387 (2016) 190–201.
[58] Y. Wang, et al., Fe/Co decorated C@CNTs derived from bimetallic metal-organic-framework for microwave absorption with wide bandwidth, J. Alloys Compd. 967 (2023) 171645.
[59] Y. Zare, M.H. Shams, M. Jazirehpour, Tuning microwave permittivity coefficients for enhancing electromagnetic wave absorption properties of FeCo alloy particles by means of sodium stearate surfactant, J. Alloys Compd. 717 (2017) 294–302.
[60] K. Sun, et al., Microwave absorption performance of magnetic-dielectric Fe3O4@C@PPy composites with a core-double-shell structure prepared by a low-temperature self-propagation method, Ceram. Int. 49 (22, Part B) (2023) 35782–35791.
[61] X. Zeng, et al., Electromagnetic microwave absorption theory and recent achievements in microwave absorbers, Carbon 168 (2020) 606–623.
[62] A. Houbi, et al., Microwave absorbing properties of ferrites and their composites: a review, J. Magn. Magn Mater. 529 (2021) 167839.
[63] H.-B. Zhao, et al., Ultralight CoNi/rGO aerogels toward excellent microwave absorption at ultrathin thickness, J. Mater. Chem. C 7 (2) (2019) 441–448.
[64] B. Zhao, et al., Synthesis of flower-like CuS hollow microspheres based on nanoflakes self-assembly and their microwave absorption properties, J. Mater. Chem. A 3 (19) (2015) 10345–10352.
[65] Y. Zhao, et al., Simultaneous optimization of conduction and polarization losses in CNT@NiCo compounds for superior electromagnetic wave absorption, J. Mater. Sci. Technol. 166 (2023) 34–46.
[66] Z. Jia, et al., Tunable Co/ZnO/C@MWCNTs based on carbon nanotube-coated MOF with excellent microwave absorption properties, J. Mater. Sci. Technol. 127 (2022) 153–163.
[67] L. Ding, et al., Ultra-broadband and covalently linked core–shell CoFe2O4@PPy nanoparticles with reduced graphene oxide for microwave absorption, J. Colloid Interface Sci. 595 (2021) 168–177.
[68] M. Jazirehpour, S.A.S. Ebrahimi, Synthesis of magnetite nanostructures with complex morphologies and effect of these morphologies on magnetic and electromagnetic properties, Ceram. Int. 42 (15) (2016) 16512–16520.
[69] M. Jazirehpour, S.A. Seyyed Ebrahimi, Carbothermally synthesized core–shell carbon–magnetite porous nanorods for high-performance electromagnetic wave absorption and the effect of the heterointerface, J. Alloys Compd. 639 (2015) 280–288.
[70] X. Li, et al., *Fabrication of three-dimensional flower-like heterogeneous Fe_3O_4/Fe Particles with tunable chemical Composition and microwave absorption performance*, ACS Appl. Mater. Interfaces 11 (21) (2019) 19267–19276.
[71] F. Yan, et al., An ultra-small NiFe2O4 hollow particle/graphene hybrid: fabrication and electromagnetic wave absorption property, Nanoscale 10 (6) (2018) 2697–2703.
[72] F. Yan, et al., Growth of CoFe2O4 hollow nanoparticles on graphene sheets for high-performance electromagnetic wave absorbers, J. Mater. Chem. C 6 (47) (2018) 12781–12787.
[73] Z. Ma, et al., Attractive microwave absorption and the impedance match effect in zinc oxide and carbonyl iron composite, Phys. B Condens. Matter 406 (24) (2011) 4620–4624.
[74] Z. Ma, et al., A new method to calculate the degree of electromagnetic impedance matching in one-layer microwave absorbers, Chin. Phys. Lett. 29 (3) (2012) 038401.
[75] P. Liu, Z. Yao, J. Zhou, Controllable synthesis and enhanced microwave absorption properties of silane-modified Ni0.4Zn0.4Co0.2Fe2O4 nanocomposites covered with reduced graphene oxide, RSC Adv. 5 (114) (2015) 93739–93748.
[76] H. Wu, et al., Co2+/Co3+ ratio dependence of electromagnetic wave absorption in hierarchical NiCo2O4–CoNiO2 hybrids, J. Mater. Chem. C 3 (29) (2015) 7677–7690.